Chemical Engineering Science 277 (2023) 118880

Contents lists available at ScienceDirect

Chemical Engineering Science

journal homepage: www.elsevier.com/locate/ces

Evolution of the pore structure-transport relationship during catalyst reduction and sintering studied by integrated multi-scale porosimetry and multi-modal imaging

Suleiman Mousa[a], Vladimir Novak[b], Robin S. Fletcher[c], Gordon Kelly[c], Monica Garcia[c], Norman Macleod[c], Christopher Parmenter[d], Sean P. Rigby[a,*]

[a] Department of Chemical and Environmental Engineering, Faculty of Engineering, University of Nottingham, University Park, Nottingham NG7 2RD, UK
[b] Swiss Light Source, Paul Scherrer Institut, Forschungsstrasse 111, 5232 Villigen PSI, Switzerland
[c] Johnson Matthey, P.O. Box 1, Belasis Avenue, Billingham, Cleveland TS23 1LB, UK
[d] Nanoscale and Microscale Research Centre, University of Nottingham, University Park, Nottingham NG7 2RD, UK

ARTICLE INFO

Keywords:
X-ray computed tomography
FIB SEM
Bulk condensation
Adsorption
Porosity
Diffusion

ABSTRACT

Catalyst pellet fabrication parameters significantly impact final product performance. Tabletted pellets are complex, hierarchical structures that evolve differently over various levels during subsequent processing. Multi-scale porosimetry and multi-modal imaging can, together, encompass all length-scales involved, and, therefore, fully characterise the evolving pellet structure during catalyst reduction and sintering. A random pore-bond network model has highlighted the key pellet structural features determining mass transport, and, thence, was predictive of the impact on mass transfer of controlled modifications to the void space for reduced and aged catalysts. Particular macroporosity, newly induced by reduction and sintering, was critical to mass transport out of proportion to its pore volume fraction. Combined X-ray tomography imaging and percolation modelling showed that reduction and sintering leads to a change (compared to the fresh state) in the initial pellet fabrication parameter that controls mass transport in pellets formed with roll-compacted feed.

1. Introduction

Many chemical processes involving heterogeneous catalyst pellets are diffusion-limited, and, thence, the overall rate is controlled by mass transfer within the pellet void space (Twigg, 2014). Porous catalyst pellets undergo a series of stages, during manufacture and usage, within which the pore structure evolves. The extent and nature of that structural evolution depends upon the characteristics of the pellet raw materials, and fabrication or process conditions. In order to optimise the many different processing parameters, during manufacture and usage, it is necessary to understand how the pore structure evolves, and how that affects mass transport rates, during each stage so that these changes can be related back to such parameters. The various stages in pellet manufacture and usage potentially include feed production, pellet forming, drying and calcination, catalyst reduction, and time on-stream in the reactor.

Many studies consider the impact of catalyst preparation conditions on final catalytic activity and lifetime, but often just consider the empirical correlation between process parameters and catalyst performance, without studying the underlying physicochemical mechanisms for the observed relationship. In the past, when the evolution of the pore structure was monitored, this was typically done just in terms of the one-dimensional, overall specific surface area or pore size distribution descriptors, or with limited sampling volume via TEM or SEM images (Schumann et al., 2014; van den Berg et al., 2016). However, the evolution of particle pore structure, during some of the stages of manufacture, has been studied in more detail, and for larger sample volumes, using CXT. The impact of different conditions for calcination of silica-alumina catalyst pellets has been considered (Tariq, Haswell et al., 2011; Tariq, Lee et al., 2011). The CXT data demonstrated that calcination at higher temperatures caused greater reduction to, and disconnection of, porosity, with changes to pore morphology due to sintering of the solid. Image analysis demonstrated that sintering caused more constrictions to arise within the void space.

However, contrasting results, concerning morphological change during the calcination of bidisperse (meso- and macro-porous), dried gel

---

* Corresponding author.
E-mail address: sean.rigby@nottingham.ac.uk (S.P. Rigby).

https://doi.org/10.1016/j.ces.2023.118880
Received 8 February 2023; Received in revised form 3 May 2023; Accepted 11 May 2023

alumina and nickel/alumina particles, were found using combined in-situ hard X-ray ptychography (XRP), 3D ptychographic X-ray computed tomography (PXCT) and hard X-ray nanotomography (Weber et al., 2022). In-situ XRP enabled the pore structural changes, during calcination at different temperatures, for samples of nickel/alumina dried gel of size 18 × 13 × 5 μm to be followed with a spatial resolution of 67.2 nm (while image pixel resolution was 18.6 nm) (Weber et al., 2022). These in-situ 2D XRP studies showed that calcination led to reduction in the overall width of the initial sample fragment, but the macroporosity seemed to, qualitatively, remain unchanged (Weber et al., 2022).

In addition, the calcination of ~15 μm particle size nickel/alumina and ~50 μm sized alumina samples were also followed using ex-situ PXCT by periodically removing samples from the calciner (Weber et al., 2022). The voxel sizes of the phase contrast tomograms of the nickel/alumina dried gel and calcined samples were ~20 and ~28 nm, respectively, with corresponding spatial resolutions, estimated by Fourier shell correlation (FSC), of ~91 and ~56 nm, respectively (Weber et al., 2022). While the voxel sizes for the dried gel and calcined alumina only samples were ~28 and ~20 nm, respectively, with corresponding estimated FSC resolutions of ~50 and ~41 nm, respectively. The PXCT enabled a direct 3D visualisation of the macropore network for pores larger than the voxel resolution. These images showed that calcination caused a decrease in the typical macropore sizes for both types of material. However, the measures of pore network connectivity and tortuosity showed no changes, thereby confirming the result from XRP suggesting there was no macropore opening, closing, or disconnection. Further, 3D maps of electron density of the mesoporous solid matrix from PXCT allowed the mapping of the spatial variation of the total (not just surface accessible) mesoporosity with pore sizes too small to be imaged directly (Weber et al., 2022). These PXCT maps suggested that calcination caused the mesoporous matrix to become denser, leading to a loss of mesoporosity However, the correlation of electron density with mesoporosity requires that the chemical composition of the intrinsic solid matrix is known, and that this composition is spatially homogeneous. Hence, the mesoporosity measurement can be inaccurate due to the presence of contaminants (such as those residues often remaining following material syntheses). In addition, measurements of electron density in regions at the sample surface are prone to artefacts because of surface defects. Some of these issues may be resolved by the use of high-density contrast agents, as will be described below.

Hondo et al. (2016) studied sintering during calcination of alumina compacts, made using feed consisting of spray dried (SD) granules, using CXT and SEM. They anticipated, based upon well-known pore-particle size ratio effects and pore stability theory, that there would be significant differences between the pore evolution of small and large pores, and, indeed, this is what they found. The CXT images showed that the larger (>5 μm) inter-granule pores increased in size with increased calcination temperature. It was also found that the finer porosity within the granules must have been eliminated, as the individual granules shrank in size.

More recently Venkatesh et al. (2023) studied the sintering of porous alumina compacts with nanotomography, using a phase-contrast holotomography set-up on a synchrotron. This system could image the ~8 mm diameter compacts with a pixel size of 25 nm for a field-of-view of 64 × 64 × 54 μm^3. However, a full-sized pellet still contains ~10^6 such sample volumes, which limits the sample volume that can be practicably studied for even just one pellet. Nevertheless, the high resolution imaging permitted the more direct sizing of larger mesopores and the determination of pore connectivity directly, including the specific identification of relatively larger pore necks. As a result, unexpected findings were obtained, such as that the shapes of the pore size distributions remained of similar form, mean size and spread, up to relatively long calcination times, and, thence, even up to higher pellet densities.

Previous work (Ruffino et al., 2005) has used CXT to probe macroporous materials containing low melting point alloy (LMPA), to aid the construction of a non-random pore bond network model, such that it could incorporate the heterogeneity in the spatial distribution of pore size observed in CXT images of empty pellets (Ruffino et al., 2005). The observed heterogeneities included a continuous ring of larger macropores within the middle of, and concentric with, the annular cross-section the hoop-shaped pellet, and also some more isolated larger macropores. A trial network model would predict a specific incidence of intrusion of pores of different sizes in the model, for a particular chosen PSD and pore connectivity, and this can be corroborated using equivalent data directly measured from CXT images. If the predictions for the appearance of the images slices is validated, then so are the underlying model parameters.

Imaging alone always requires a trade-off between the sampled field-of-view and the image resolution (Arif et al., 2020). However, this disadvantage of direct imaging methods can be off-set by combining with the more representative data from indirect methods. In previous work, an integrated series of gas sorption, mercury porosimetry and multi-modal imaging has been used to study a variety of porous materials, including catalyst supports (Rigby et al., 2004), cements (Qian et al., 2018; Zeng et al., 2020; Qi et al., 2021) and rocks (Fusi and Martinez-Martinez, 2013; Seely et al., 2022). More recently, this method has been used to study the initial feed particles and compacted pellets of copper-zinc oxide-alumina, methanol synthesis catalysts made using either roll-compacted or spray-dried feed particles (Mousa et al., 2023). The imaging of the formed pellets, using CXT at two different resolutions along with FIB-SEM, showed that they possessed a complex hierarchical structure, with some fractal features. The individual feed particles were still evident in the large-scale images of the whole pellets. Higher resolution imaging revealed that the initial feed particles were also composite materials. The internal structure of the roll compacted feed particles thus resembled that of the larger finished compact, such that the pellets demonstrated a fractal character. The spray dried feed particles were, also, themselves composed of smaller spherical particles of variable density. Some of these constituent particles were of very high density throughout, while other particles consisted only of high density shells surrounding large macroporous voids (denoted 'bubble pores'). Similar large voids have been found previously, also using CXT, in fluid catalytic cracking (FCC) particles made by spray-drying, and so these voids seem a common feature of the method (Bare et al., 2014).

Minimalist idealisation models of the pore structure of amorphous catalyst pellets are of only the degree of complexity necessary to include the particular causal factors which give rise to the phenomenon of interest, namely mass transport, occurring within the porous solid (Weisberg, 2013; Rigby, 2023). Hence, only those features of the void space structure that 'make a difference to the occurrence or essential character of the phenomenon in question' are included (Weisberg, 2013). The so-called 'sifting' or 'filtering' strategy can be used to identify these particular features (Rigby, 2020, 2023). The integrated gas sorption and mercury porosimetry experiments can be used to implement this strategy to examine the differential importance of various specific bins in pore size, and pores associated with particular aspects of the pellet microstructure (such as the aforementioned 'bubble pores'), to mass transport (Mousa et al., 2023). In this approach different elements of the void space were 'knocked-out' of the pore network in a controlled way, using mercury entrapment, and their importance was then assessed by the impact of their loss on subsequent phase transitions and mass transport rates (Rigby et al., 2004; Nepryahin et al., 2016; Hill-Casey et al., 2021). CXT was used to image the spatial distribution of entrapped mercury following porosimetry scanning curve experiments up to various ultimate intrusion pressures to fill progressively more pores (Mousa et al., 2023). These images showed that the spatial pattern of mercury ingress was different for the two sorts of pellet formed with different feed types. The pattern of entrapped mercury in the spray dried feed pellets exhibited a shrinking-core effect whereby a front of mercury gradually advanced radially into the pellet with increasing intrusion pressure. In contrast, the mercury entrapment for the roll-compacted pellets showed initial intrusion in a band around the circumference of the pellet, but, soon thereafter, intrusion was in the form of dendritic branches extending into the centre of the pellet. However, despite the differences in the spatial disposition of entrapped mercury with pellet type and for variable mercury saturation, the change in the rate of transient gas uptake induced by the entrapped mercury was still predictable using a simple random bond percolation model for the partially mercury-saturated network. The model parameters were obtained using percolation analysis of gas sorption data derived from the overcondensation method, which is a special technique that allows gas sorption to probe macroporous systems (Murray et al., 1999). It was found that the relative rise in pellet tortuosity increased linearly with the relative rise in model lattice size, as mercury saturation increased. The CXT data showed why this simple model worked despite the complexity of the observed patterns of entrapment. The apparent lattice size obtained from the percolation analysis depends upon the roundedness of the desorption knee, which, for random systems, is related to the incidence of surface clusters of large pores which desorb earlier than the main percolation transition. If these surface clusters are blocked, then the lattice size appears to increase. The CXT images showed that both spray-dried and roll-compacted feed pellets possessed surface clusters of larger pores, intruded and blocked with mercury at low pressures. Hence, when these were blocked by mercury, the general accessibility of the network was reduced, forcing the diffusive flux to take a more circuitous route into the pellet. This demonstrated the importance of ensuring these surface clusters are generated in the pellet fabrication process to ensure good mass transport properties. In this work, it will be seen that these clusters of larger pores become even more critical to mass transport following catalyst reduction.

Previous work (Mousa et al., 2023) considered the early stages of the life-cycle of the methanol synthesis catalyst, while this work will look at the very different later stages of the life-cycle. It is the purpose of this work to study how this pellet pore structure evolves during catalyst reduction, and during use on-stream in the reactor as the catalyst becomes aged due to sintering. These new data, for reduced and aged samples, will also provide a test of the percolation model, developed for fresh pellets, based upon a random lattice comprised of the critical elements of the pellet structure for mass transport. It will be seen that this model will make a novel prediction of a change in critical structural element for aged catalysts that is subsequently confirmed by independent evidence from CXT. CXT studies of entrapped mercury following porosimetry, used to progressively modify the void space in a controlled way, will be employed to show how the external accessibility of the void space of catalyst pellets is changed by reduction and sintering, due to the induction of macroporosity via solid shrinkage and re-organisation. Given the creation of new macropores, this work will demonstrate the particular utility of gas overcondensation, given its capability of characterising the whole macro-mesopore network with one single experimental technique, such that the whole pore network can be analysed together using percolation methods. This work shows how the so-called sifting strategy (Rigby, 2020) is a suitable approach for dealing even with highly hierarchically-heterogeneous pellets, as studied here.

Table 1
Characteristics of the reduced and aged catalyst pellets. Porosity and bulk density values were obtained from mercury porosimetry-helium pycnometry.

Sample	Porosity/ %	Bulk density/(g/ cm^3)	Cylinder dimensions (diameter × height)/mm
Reduced SD	67.3	1.91	5.5 × 3.4
Aged SD	69.4	1.92	5.4 × 3.4
Reduced RC	64.4	1.80	5.4 × 3.5
Aged RC	65.1	2.10	5.6 × 3.4

2. Theory

Mass transport properties can be characterised by kinetic gas uptake experiments. Kinetic mass uptake data, comprising amount adsorbed versus time, typically takes the mathematical form of an exponential growth, and, thus, is often fitted to the so-called Linear Driving Force (LDF) model (Rigby, 2020). The characteristic parameter of this process is the mass transfer coefficient, denoted k. The LDF k-value is defined by the function (Rigby, 2020):

$$M = M_0\left(1 - e^{-kt}\right) \tag{1}$$

where M the amount of nitrogen adsorbed at time t, M_0 is the ultimate total adsorbed amount of nitrogen for the adsorption pressure point, and k is the mass transfer coefficient. The apparent mass transfer coefficient, obtained from a fit to raw uptake data, must be corrected for the effect of concurrent adsorption using the slope of the isotherm at the relevant adsorption pressure point. In this way the actual mass transfer coefficient is obtained.

For a porous sample, the mass transfer coefficient k depends upon the intrinsic effective diffusivity of the porous material, composed of the reference diffusivity D_A, the porosity (voidage fraction) and tortuosity of the medium, plus the diffusion penetration depth a, and a geometric factor G, which is 15 for a spherical particle and 8 for a cylinder (Rigby, 2020):

$$k = \frac{GD_A\frac{\varepsilon}{\tau}}{a^2} \tag{2}$$

The reference diffusivity will be the bulk molecular diffusivity in the molecular diffusion regime, and the Knudsen diffusivity for the critical pore size in the Knudsen regime. If a fraction of a porous network is removed in some manner, but the reference diffusivity and the particle overall size and geometry remain constant, then the ratio of the original tortuosity τ_0 to the subsequent tortuosity τ will be given by:

$$\frac{\tau_0}{\tau} = \frac{k}{k_0}\frac{\in_0}{\in} \tag{3}$$

where the subscript 0 denotes the parameter for the original porous network and the lack of subscript represents the general parameter for any modified network. The concept of tortuosity is a complex one, and has been reviewed extensively previously (Ghanbarian et al., 2013; Carniglia, 1986; Epstein, 1989). However, in this work, the definition used is a so-called ‘physical tortuosity’, as it is based explicitly upon a transfer process (Fu et al., 2021). It is noted that, while surface diffusion can be important in catalysis under reaction conditions (e.g. Rieckmann and Keil, 1998), where it can constitute a large fraction of the mass transport flux, it is not important in the gas uptake experiments below, since they were conducted at low pressure where the surface coverage is very low, and thus the surface diffusion flux is also correspondingly low. However, the influence of coupled diffusion and adsorption was taken into account.

The macroscopic structure of the catalyst pellets studied in this work was modelled by three-dimensional, random pore bond networks. This type of model consists of a lattice of cylindrical, pore bond elements that join at lattice node junctions. The typical number of pore bonds meeting at a node, averaged over the whole lattice, is denoted the pore connectivity Z. The overall size of the lattice measured in lattice bond units is called L. The model parameters Z and L were determined from percolation theory-based analysis of gas sorption data using a method based upon that developed by Seaton (1991), as extended, to include the potential variation of pore length with pore diameter, by Rigby et al. (2004), and described in earlier work (Mousa et al., 2023).

Table 2
Specific pore volumes and modal pore diameters of the samples as determined by two different methods.

Sample	Hg pore volume/(ml/g)	N_2 sorption pore volume/(ml/g)	Hg modal macropore diameter/(nm)	N_2 modal mesopore diameter/(nm)
Reduced SD	0.324	0.356	37.5	10.9
Aged SD	0.333	0.340	60.3	20.8
Reduced RC	0.322	0.332	35.9	11.7
Aged RC	0.315	0.321	51.0	19.1

3. Materials and methods

3.1. Catalyst samples

Reduced and aged methanol synthesis catalyst pellets, made using either spray-dried (SD) or roll compacted (RC) feed materials, as described in detail previously (Mousa et al., 2023), were studied in this work. Fresh catalyst samples (as used in previous work by Mousa et al. (2023)) were reduced with a flowing gas mixture (20,000 $l.\mathrm{hr}^{-1}.\mathrm{kg}^{-1}$) containing 2 vol% hydrogen, with the balance as nitrogen, held at a temperature of 225 °C for 8 h, at ambient pressure. The aged pellets were provided by Johnson Matthey. The SD and RC pellets are mesoporous cylindrical tablets with dimension of 5.4 × 3.4 mm (base diameter × length) (see CXT images). Tables 1 and 2 provide details on the other relevant properties of the samples studied.

3.2. Integrated mercury porosimetry and gas sorption

The integrated mercury porosimetry and gas sorption technique consists of a series of experiments conducted on the same sample. The nitrogen sorption isotherms were measured at liquid nitrogen temperature (77 K) using a Micromeritics 3Flex physisorption analyser. Approximately 0.8 g of the sample (4 cylindrical pellets) was weighed and placed into a pre-weighed standard physisorption sample tube with a sealing frit placed at the top to prevent the sample from being evacuated into the 3Flex manifold. The tube (with sample) was then loaded into the degassing station and initially degassed at room temperature until a vacuum of 0.02 mmHg was reached. The sample temperature was then raised to 140 °C by using a heating mantle, and the sample was left under vacuum for 24 h. The thermal pre-treatment drives off any physisorbed water on the sample but does not change the sample morphology. After the 24 h had passed, the heating mantle was removed, and the sample was allowed to cool down to room temperature. The sample tube and its contents were then re-weighed to obtain the dry weight of the sample. Isothermal jackets were then placed around the sample tubes before reattaching them to the analysis port to begin the automated gas sorption analysis. The isothermal jacket ensures a constant thermal profile of 77 K along the length of the sample tube during the analysis stage. Nitrogen purity was 99.995%. The isotherms consisted of approximately 60 adsorption and 50 desorption points. Gas sorption was measured over the relative pressure (P/P_0) range of 0.01 to 0.995 for adsorption isotherm and 0.995 to 0.10 for desorption isotherm. The saturation pressure (P_0) was measured for each data point on the isotherm.

Once the first nitrogen gas sorption experiment was finished, the samples were allowed to reach room temperature (~295.15 K) and then quickly transferred to a mercury intrusion porosimetry (MIP) machine to entrap mercury into the pores. Mercury intrusion and retraction curves were measured using a Micromeritics Autopore IV 9500, which can generate a maximum pressure of 414 MPa (60,000 psia). Mercury intrusion data was generated for the range specified in the scanning curve pressure points followed by retraction back down to atmospheric pressure. The sample was transferred into a penetrometer, and the weight of the penetrometer and sample was recorded. The penetrometer (with sample) is then placed in the low-pressure port of the instrument. During the low-pressure analysis, the sample is evacuated up to 50 μmHg to drive off any water vapour or atmospheric gases in the pore network. The sample bowl is then filled with mercury while the entire system is still under low pressure. Data collection begins at a pressure of 0.5 psia, which is enough to cause mercury to penetrate sample pores larger than 360 μm in diameter. After the low-pressure analysis was completed, the assembly weight (penetrometer + sample + mercury) was recorded, the penetrometer was transferred to the high-pressure port, and the chamber was closed tightly. The penetrometer is placed vertically in the high-pressure port, and it is surrounded by oil, which is the hydraulic fluid the instrument uses to generate high pressures. As the hydraulic fluid pressure rises, it is transmitted to the mercury in the penetrometer via its open capillary stem. An equilibration time of 15 s was used for each data point.

Once the mercury intrusion experiment was finished, the sample was immediately discharged from the penetrometer, recovered, and returned to the 3Flex sample tube, where the rate of adsorption and the conventional adsorption experiments were repeated. The sample was first cooled to 77 K by manually raising the Dewar flask, allowing the sample to freeze for approximately 30 min. This part was crucial in the post mercury entrapment steps since it freezes the mercury in-place to ensure that it all remains immobilised within the pellets. The integrated rate of adsorption-mercury porosimetry aims to selectively block specific pore sizes and then study how important those pores were to the rate of mass transport before and after their removal. Previous experiments where the mercury was thawed and re-frozen after a week prior to subsequent gas sorption have shown that the mercury ganglia did not move around over this timescale or due to the freezing since the shapes of the gas sorption isotherms remained the same (Nepryahin et al., 2016).

3.3. Rate of adsorption (ROA) procedure

The rate of adsorption technique works by dosing a known quantity of nitrogen gas onto the sample and then recording the amount of gas adsorbed and the corresponding pressures over time. The dosing quantity was taken from the BET monolayer capacity (V_m). An additional 5 cc of gas was added to this amount to compensate for the initial expansion of the gas into the free space of the sample tube. This is because the gas first fills the sample tube before adsorbing onto the sample surface. The number of readings of pressure was set at 1000 readings per dose. The ROA data was collected at the lowest pressure point in the isotherm. In this region of the isotherm, there is negligible obstruction from adsorbed phase, and the diffusion is in the Knudsen regime and corresponds to the process conditions in the reactors in which the methanol synthesis pellets are used. The rate of uptake data was collected both before and after mercury entrapment.

3.4. Overcondensation gas sorption procedure

The nitrogen overcondensation (OC) experiment was carried out on a Micromeritics ASAP 2020 physisorption analyser. The OC experiment is explained in more detail in previous work (Mousa et al., 2023) and uses a method similar to that described by Murray et al. (1999). The OC experiment involves "flooding" the sample chamber with condensed liquid nitrogen to submerge the sample in liquid nitrogen to investigate any porosity beyond the instrument upper limit for the conventional isotherm ($P/P_0 > 0.995$). The conventional isotherms for these materials clearly show that porosity exists beyond the conventional instrument's upper limit. Once the sample is fully submerged in liquid nitrogen and total pore filling is achieved, the pressure in the tube is lowered to just below the saturated vapour pressure of nitrogen such that the bulk condensate vapourised completely while all the sample internal porosity is liquid-filled. Once this step has been achieved, the first data point on

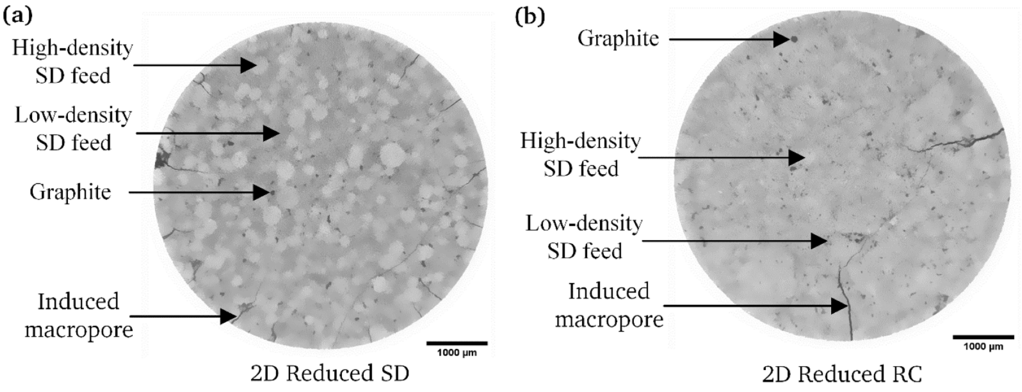

Fig. 1. Raw 2D radial slice CXT images for the (a) Empty reduced SD, and (b) Empty reduced RC feed pellet.

the overcondensation desorption isotherm can be measured. This point corresponds to the total pore volume of the sample. The pressure is then progressively lowered in small steps, and the rest of the desorption isotherm was obtained in the usual way. The reported raw data (relative pressure and volume adsorbed (cc/g STP)) is greatly offset to what would be expected due to the very large amount of gas (from the bulk liquid nitrogen) that must be removed before the onset of desorption from the sample porosity. The data were normalised to a quantity of gas on the adsorption isotherm below a relative pressure of 0.42 where, for the conventional isotherm, the desorption data coincides with the adsorption data. The OC data was collected for the samples both before and after mercury intrusion.

3.5. Computerised X-ray tomography and focussed ion beam scanning electron microscopy (FIB-SEM)

3.5.1. Low resolution computerised X-ray tomography (CXT)

For the low-resolution CXT scans, the pellets were imaged before and after mercury entrapment using a Zeiss Xradia Versa XRM-500 to acquire 3D image stacks. The X-ray source for the Xradia 500 Versa instrument was set to 140 kV and power of 10 W. The apparatus's macro lens (0.4X) was used to image the whole pellets with a diameter of 5.4 mm with 360 degrees rotations. The average pixel size for empty pellets was 5.6 μm, and the average pixel size for samples with mercury was 5.9 μm. Image acquisitions parameters were the same for all the empty samples and the samples with entrapped mercury. The scan times were roughly 2 h for the empty samples and 2.5 h for mercury-filled pellets. Both samples were scanned with 1600 projections per 360 degrees scan. Each 3D image stack contained 1016 slices with dimensions of 1024 × 1024 pixels and 24-bit depth.

3.5.2. High resolution computerised X-ray tomography (CXT)

Multi-scale imaging of the feed materials was performed by X-ray tomography at the TOMCAT beamline (Swiss Light Source). The high-resolution microscope (Optique Peter), with 4×, 10 × and 20 × magnification and LuAG:Ce 20 μm scintillator, was used in combination with a Pco.Edge 5.5 detector, yielding an effective pixel size of 1.63, 0.65 and 0.325 μm, respectively. Spray-dried (SD) feed material was scanned with an energy of 20 keV and 150 ms exposure time per projection. Monochromatic energy of 30 keV and an exposure time of 500 ms were used to acquire images of bigger roll compacted (RC) particles. Both samples were scanned with 2500 projections per 180 degrees scan. The 3D volume data sets were reconstructed using the propagation-based phase-contrast method (Paganin et al., 2002) and the gridrec algorithm (Marone and Stampanoni, 2012).

3.5.3. Focussed ion beam- scanning electron microscopy (FIB-SEM)

The serial milling images were acquired using a Crossbeam 550 (Carl Zeiss Microscopy, Oberkochen, Germany) instrument equipped with a cryo-stage (QT3010, Quorum Technologies, Lewes, UK) and vacuum transfer system for FIB-SEM imaging. The samples were mounted onto the cryo-shuttle two at a time, and transferred into the Crossbeam 550 from a glovebox (argon) fitted with a Quorum Technologies 3004 QuickLok port using the Quorum transfer rod.. Once the samples were inside the instrument, an automated FIB milling algorithm (serial sectioning) was subsequently set up and executed. To ensure that the unsupervised automated FIB milling was successful, the equipment was properly aligned and calibrated on a weekly basis. Following deposition of a platinum protection layer the Crossbeam 550 was programmed to mill a cross-section with dimensions of 10 × 30 × 10 μm (XYZ) through the sample to acquire a 3D image stack. A fixed voltage of 30 kV and a current of 700 pA was used to generate the FIB slices. SEM images were acquired at an accelerating voltage of 2 kV and 100 pA.

3.5.4. Image analysis

The image analysis and segmentation were carried out in Dragonfly ORS software using a deep learning neural network (Makovetsky et al., 2018). For the segmentation of the high- and low-density SD CXT images, a U-Net (Ronneberger et al., 2015) convolutional neural network was used with a patch size of 32 × 32 pixels, a stride to input ratio of 0.5, a batch size of 32, the loss function ‘OrsDiceLoss, and an optimisation algorithm of Adadelta (Zeiler, 2012). For the training dataset, 20 of the 1016 pre-processed 2D image slices were selected and manually delineated to identify each pixel with one of three phases: graphite, low-density, and high-density regions. Dragonfly has tools that can be adjusted in size for the manual segmentation task, including brushes and erasers. To train the U-Net model, some of the different phases present in the training dataset were manually segmented (painted), varying according to their shape and size. The manually segmented images were subsequently used as input data for the U-Net model. After the model was trained successfully, it was applied to segment the remaining unseen images from the same CXT batches, resulting in fully segmented image stacks.

4. Results

4.1. Imaging empty SD and RC pellets

4.1.1. CXT

Fig. 1(a) and (b) show typical examples of 2D radial cross-section slice CXT images, of the empty reduced SD and RC feed pellets, respectively. The reduced SD and RC samples have a similar overall feed particle composition to that observed previously (Mousa et al., 2023) for the fresh pellets, namely a mixture of high-density and low-density feed particles indicated by the lighter and darker pixels, respectively. The sample images also contain many smaller, dark black spots, which correspond to the graphite lubricant particles. However, the reduced pellets contain induced macroporosity not present in fresh pellets

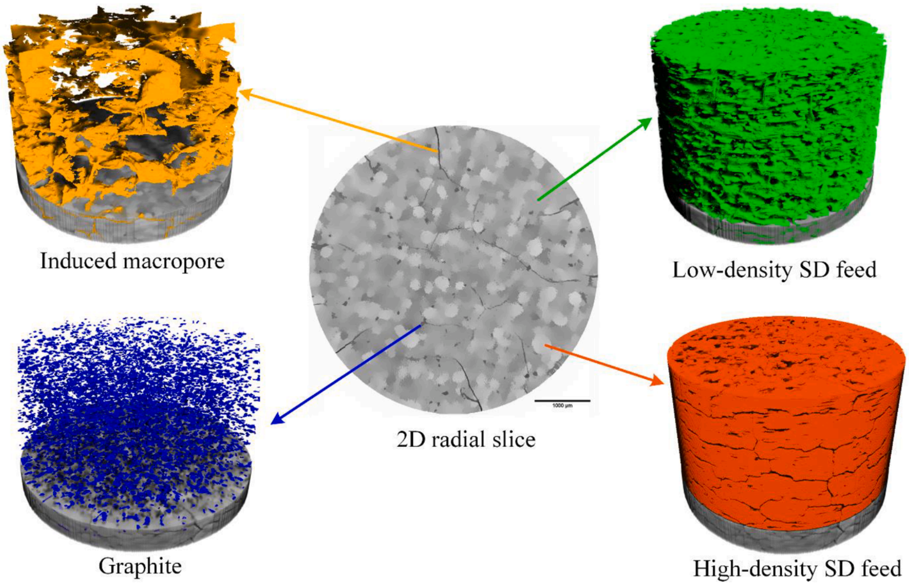

Fig. 2. Results of CXT image segmentation for empty reduced SD feed pellet, showing the spatial disposition of reduction-induced macropores, and the low density and high density feed particles, and carbon lubricant.

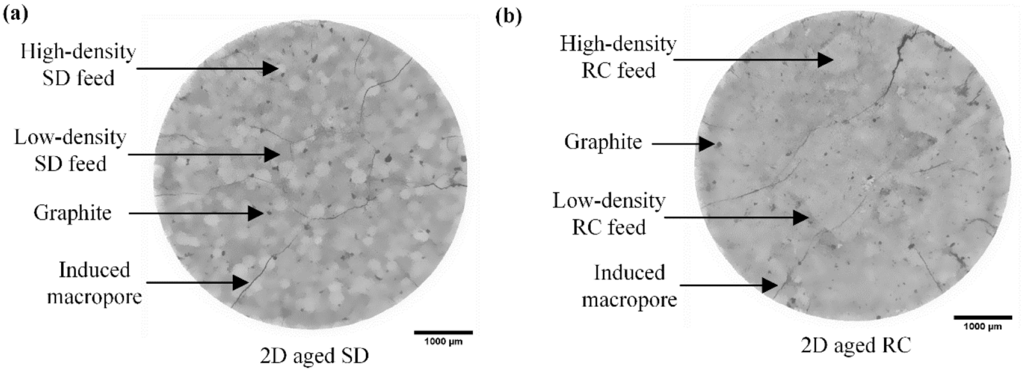

Fig. 3. Raw 2D radial slice images for the (a) Empty aged SD, and (b) Empty aged RC feed pellet.

(Mousa et al., 2023), as discussed below. In order to make the spatial distribution of these different phases more apparent, the images were segmented, and an example of the results for the reduced SD feed pellet are shown in Fig. 2.

Fig. 3(a) and (b) show examples of 2D radial cross-section slice CXT images of the empty aged SD and RC feed pellets, respectively. It can be seen, for both types of pellet (SD and RC), that the decrease in solid volume caused by reduction of copper oxide to copper metal, and then further changes, involving solid consolidation, caused by sintering of the copper, has induced the production of large macropores (henceforth referred to as induced macropores), often at the boundaries between constituent feed particles, where these have shrunken in volume. The aged SD pellets have more extensive induced macropore networks than the aged RC samples. The induced network appears to be more complex nearer to the outer layer of the pellet.

4.1.2. *FIB-SEM imaging*

Fig. 4(a) and (b) show a 2D slice SEM image and a 3D volume reconstruction from 300 slices for the reduced SD and RC pellets, respectively. The rounded, high-density (as shown by high intensity image voxel) particles found previously (Mousa et al., 2023) in the fresh SD samples are also found in the reduced SD samples. However, while these rounded particles in the fresh SD sample had no macropores within them (as revealed by the marked gap in the mapped distribution of macropores within the region of these particles in the SEM images obtained previously (Mousa et al., 2023)), in contrast, for the reduced SD sample, the number of macropores (dark spots in 2D slice in Fig. 4) seen within these denser particles has greatly increased. This is manifested in the increase in the porosity value for SD pellets from 47.1% for the corresponding fresh pellet (Mousa et al., 2023) to 67.3% following reduction, as can be seen in Table 1.

Fig. 5(a) and (b) show a 2D slice SEM image and a 3D volume reconstruction from 230 slices for the aged SD and RC pellets. In contrast to the reduced pellets, many of the macropores have changed morphology or disappeared after the ageing process. The consolidation of the solid phase on sintering contributes to the loss of the macropores in the pellet.

4.2. *Mercury porosimetry*

Raw mercury porosimetry boundary and scanning curves were obtained for the whole pellet forms of the reduced and aged, SD and RC samples, and these are shown in the Appendix. These data were then analysed using the Kloubek (1981) correlations, which are a semi-empirical alternative to the Washburn equation, to obtain pore sizes from intrusion pressure, and the resultant curves are shown in Fig. 6. The mercury intrusion data shows that, as the ultimate mercury pressure is increased, then, progressively, more intrusion occurs into the ever-

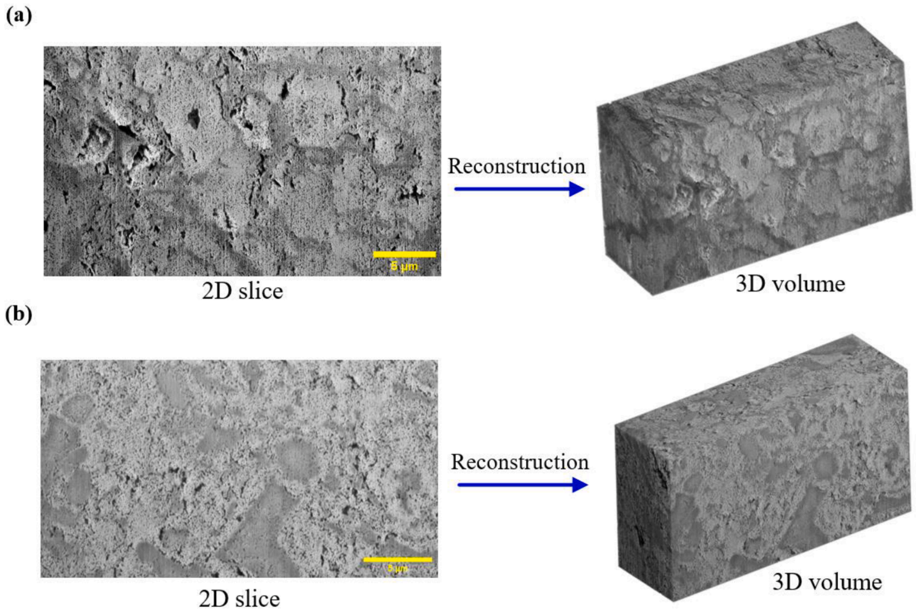

Fig. 4. 2D and 3D reconstructed grayscale FIB-SEM images for sections of the (a) Reduced SD and (b) Reduced RC samples. The scale bar corresponds to 5 μm. Higher (whiter) intensity corresponds to higher density, and darker pixels correspond to lower density.

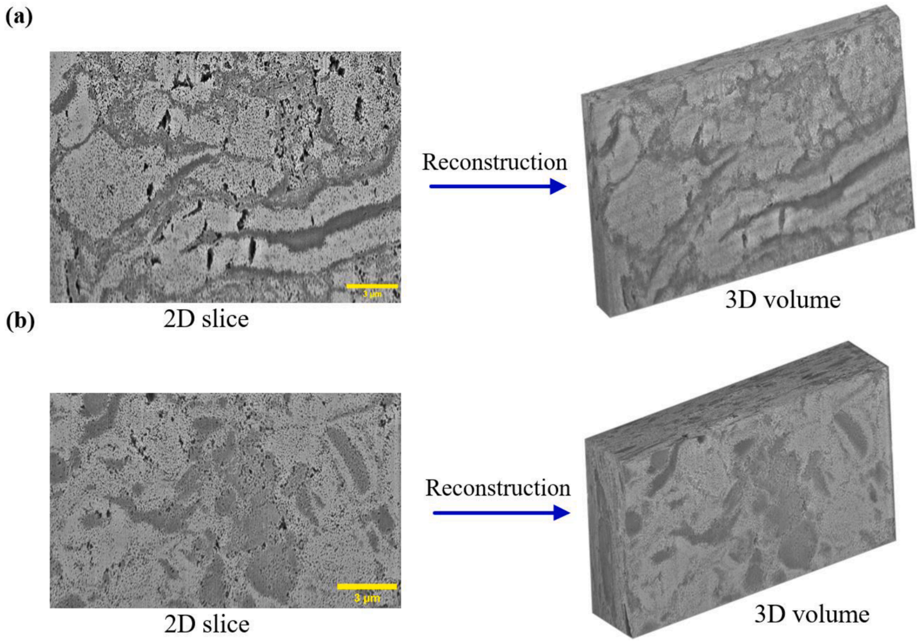

Fig. 5. 2D and 3D reconstructed grayscale FIB-SEM images for the (a) Aged SD and (b) Aged RC. The scale bar corresponds to 5 μm. Higher (whiter) intensity corresponds to higher density, and darker pixels correspond to lower density.

smaller pore necks.

The scanning curves, up to different ultimate intrusion pressures, were used to 'filter-out' specific pores sizes in a controlled way by filling them with mercury. The ultimate intrusion pressure achieved at the top of each intrusion curve indicates which pore-necks have been penetrated by mercury. The extrusion curves show what fraction of the pores that have been penetrated are still full of mercury, and, thereby, blocked out. From the mercury extrusion data, it can be seen that, typically, ~70-100% of the intruded mercury becomes entrapped, depending upon the ultimate intrusion pressure, with fractionally less mercury becoming entrapped for higher ultimate intrusion pressures. The slight shifts in pore sizes for the scanning curves reveal a small amount of intra-batch variability amongst the pellets from the same batch. By applying the Kloubek (1981) correlations to the raw data for aged samples, a superposition of the intrusion and extrusion curves was achieved for smaller mesopore sizes (<10 nm for SD and < 9 nm for RC). This creates 'swan-neck' like forms at the top of the curves for the aged SD and RC samples. Furthermore, this indicates that, for all the pore sizes below 10 nm, the cause of hysteresis was just because of the difference in contact angles between the mercury and the pore walls for the advancing and retreating mercury menisci, as described in previous work (Rigby et al., 2004). The lower parts of the porosimetry curves are, thus, dominated by structural hysteresis, as these lead to total mercury entrapment.

Hence, in summary, the noted drop in the fractional mercury

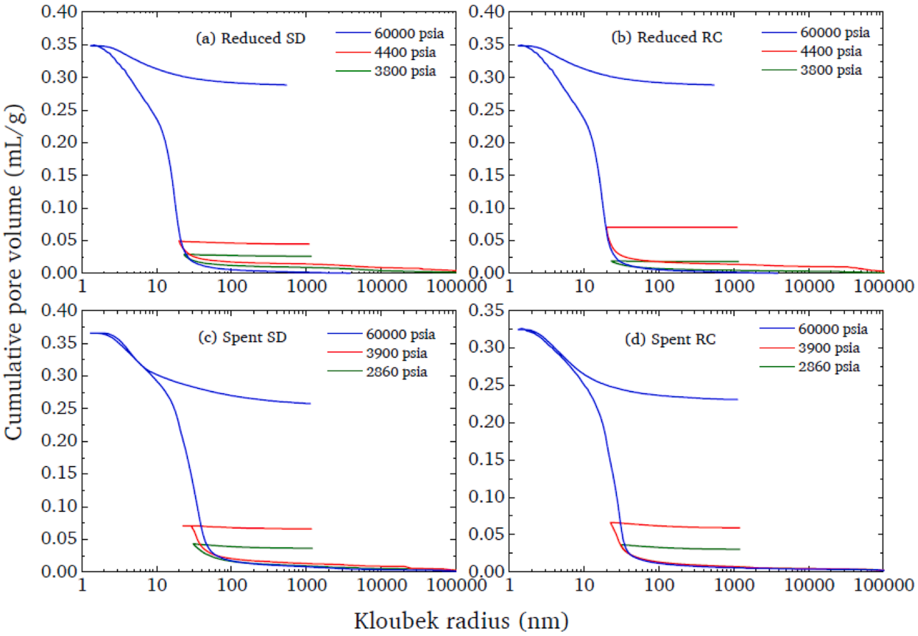

Fig. 6. Mercury porosimetry scanning curves to different indicated ultimate pressures that have been analysed using the Kloubek (1981) correlation for (a) Reduced SD, (b) Reduced RC, (c) Aged (Spent) SD and (d) Aged RC samples. The mercury scanning curve pressures are indicated on the graph legends.

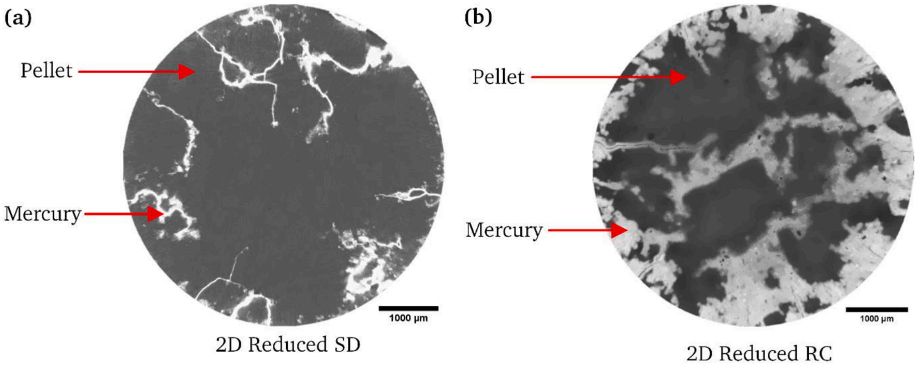

2D Reduced SD

2D Reduced RC

Fig. 7. Examples of typical 2D CXT slice images from the central region of the pellet following mercury intrusion up to 3800 psia for (a) Reduced SD, and (b) Reduced RC samples.

entrapment with increasing intrusion pressure is because, the hysteresis in the lower part (lower pressure) of the mercury intrusion curves is dominated by structural hysteresis, which causes virtually complete entrapment. However, in contrast, the hysteresis in the upper part (‘swan-neck like region) of the curve is dominated by contact angle hysteresis, and the retraction is reversible. Hence, the higher intrusion pressures result in more mercury retracted in percentage terms. It is also noted that mercury intrusion occurs at much lower pressures for the reduced and aged samples, than for the corresponding fresh samples, as seen in earlier work (Mousa et al., 2023).

4.3. CXT imaging of pellets following mercury entrapment

Fig. 7(a) and (b) show typical reconstructed 2D radial slice CXT images of the reduced SD and RC samples following mercury intrusion up to 3800 psia. Due to the very high X-ray absorbance of mercury, the regions of the pellet containing entrapped mercury appear as bright white pixels, while the empty pellet matrix appears in various shades of grey. From Fig. 7(a), it can be seen that, for intrusion up to this particular ultimate pressure, mercury penetration of the reduced SD pellet is largely limited to the induced macroporosity and the immediate environs of the wider solid matrix. This contrasts with the pattern of mercury intrusion within the fresh SD pellet seen in previous work (Mousa et al., 2023), where mercury ingress occurred as an almost continuous front, such that the region unoccupied by mercury was largely a shrinking core at the centre of the pellet. However, for the reduced RC pellet, mercury penetration is more extensive and pervasive, more like that observed previously for the fresh RC pellets (Mousa et al., 2023). The black voids in the image have similar irregular shapes to those of the constituent roll-compacted feed particles evident in the images of the fresh pellets in previous work (Mousa et al., 2023). Due to the very high retention of entrapped mercury evident in Fig. 7, it thus seems likely that, for the RC feed pellet, mercury has penetrated some constituent feed particles extensively, whereas for others, probably guarded by necks too small to penetrate at 3800 psia, no mercury entered. This suggests that extended regions of the pellet are accessible only via narrow necks, while other regions are more freely accessible. From Fig. 7, it can be seen, from the dark patches meeting the exterior surface, that free accessibility of the interior of the intruded reduced RC pellet is retained even with mercury entrapment, albeit over a much reduced external surface area.

Figs. 8 and 9 show typical examples of reconstructed 2D radial slice

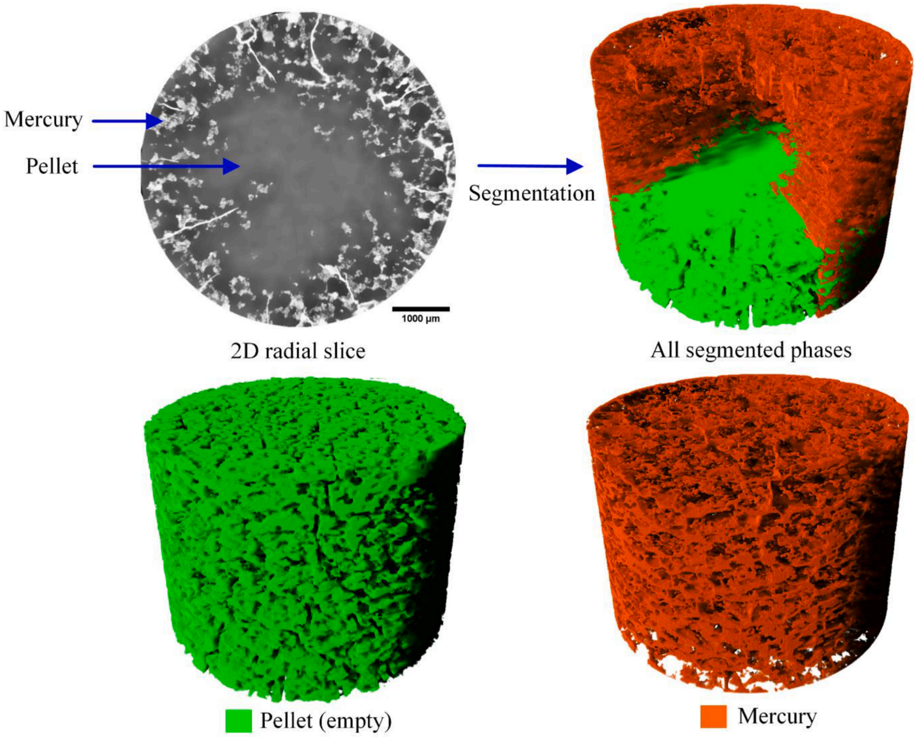

Fig. 8. 2D radial slice CXT image of the central region of an aged SD pellet, and the results of segmentation of the CXT data for the aged SD feed pellet, following mercury intrusion to 2860 psia, showing spatial disposition of mercury-containing and empty regions of pellet.

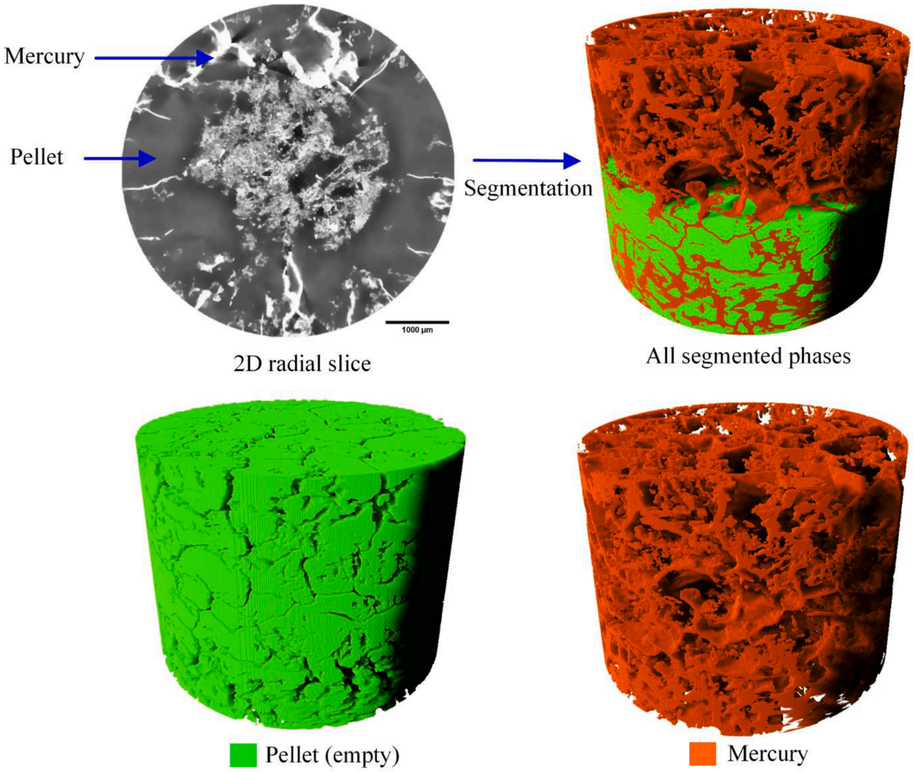

Fig. 9. 2D radial slice CXT image of the central region of an aged RC pellet, and the results of segmentation of the CXT data for the aged RC feed pellet, following mercury intrusion to 2860 psia, showing spatial disposition of mercury-containing and empty regions of pellet.

CXT images of the aged SD and RC pellets following mercury intrusion up to 2860 psia. From Fig. 8, it can be seen that mercury penetration for the aged SD pellet is more extensive, even at a lower intrusion pressure, than for the reduced SD pellet. While mercury penetration is still substantially directed along the induced macroporosity, much more partial intrusion of the surrounding, adjacent matrix is also occurring, albeit in

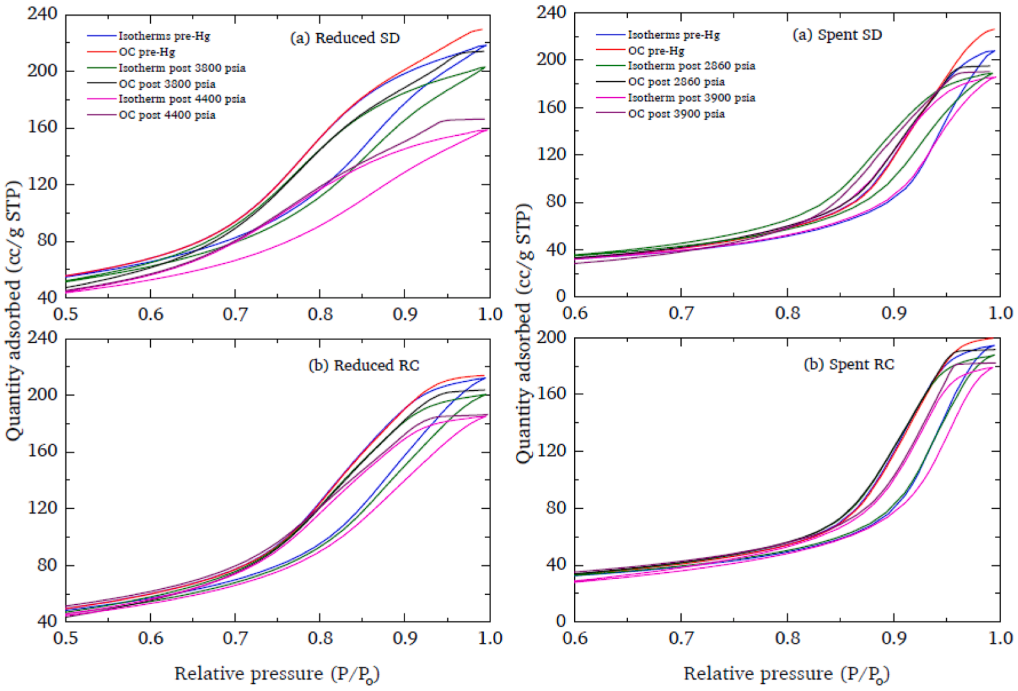

(a) Reduced SD and RC (b) Spent SD and RC

Fig. 10. Hysteresis loop region of conventional sorption isotherms and overcondensation (OC) boundary desorption isotherms for empty samples, and the samples following mercury intrusion to up to different pressures: (a) Reduced SD and RC up to 3800 and 4400 psia, and (b) Aged (Spent) SD and RC up to 2860 and 3900 psia.

a patchy pattern. It is clear, from an examination of the morphology of the intruded and unintruded regions, that some black voids are circular, and thus represent completely unintruded, higher density SD feed particles, very similar to what was observed previously for fresh pellets (Mousa et al., 2023). In contrast, the spatial pattern of mercury intrusion for the aged RC pellet is very different in geometric form to that observed for both the corresponding fresh and reduced states for this type of pellet, and for the SD pellets. While, in the outer regions of the pellet, mercury intrusion is mostly directed along the induced macroporosity, with some limited lateral intrusion into the surrounding matrix, in contrast, in the core of the pellet, the mercury distribution is much more pervasive throughout the matrix. The full CXT data-set for the whole pellet was segmented in order to make the 3D spatial distribution of entrapped mercury in the outer regions clearer, and the results are also shown in Figs. 8 and 9. For an aged RC pellet, mercury is able to flood the central core of a pellet at much lower pressures than for the

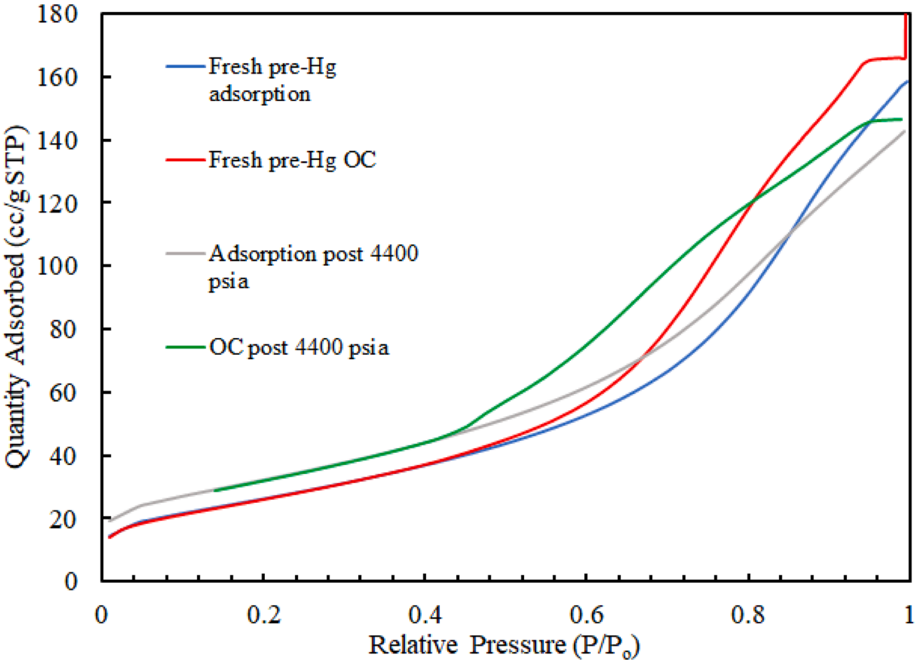

Fig. 11. A comparison of the conventional adsorption isotherms and overcondensation (OC) boundary desorption isotherms for empty (pre-Hg) fresh SD feed pellets and reduced SD feed pellets following (post) mercury intrusion to 4400 psia.

Table 3
Connectivity (Z) and lattice size (L) parameters from a percolation analysis of gas sorption data for (a) Reduced SD pellets and (b) Reduced RC pellets, both empty (pre-Hg) and following (post) mercury intrusion to different stated pressures.

Samples	(a) Reduced SD			(b) Reduced RC		
	Empty pore fraction/%	Z	L	Empty pore fraction/%	Z	L
Pre-Hg	100.0	3.63	2.95	100.0	3.51	2.87
Post 3800 psia	91.5	3.05	4.21	94.6	2.98	4.90
Post 4400 psia	85.4	2.92	4.98	85.8	2.82	5.88

other states of the RC pellets, and also contrasts markedly with the SD pellets. However, a similar pattern of mercury intrusion has been observed previously (Nepryahin et al., 2016), for fresh RC pellets that had been tabletted to a much lower density (1.93 g.cm^{-3} versus 2.3 g.cm^{-3}) than the RC pellets used here. In these low density pellets, CXT images showed that substantial macroporosity was left surrounding the individual feed particles constituting the pellet, as they had not been closed by the pelleting pressure, and these formed conduits to the pellet core. This suggests that the mercury can reach the centre of the aged pellet at low intrusion pressure via the significant macroporosity induced by reduction and sintering.

4.4. *Gas sorption isotherms*

Fig. 10 shows the conventional nitrogen sorption isotherms, and overcondensation boundary desorption isotherms, for empty reduced and aged pellets made with SD or RC feed. Also shown in Fig. 10 are the conventional and overcondensation isotherms for samples of reduced pellets following mercury intrusion to either 3800 or 4400 psia, and for samples of aged pellets following mercury intrusion to 2860 or 3900 psia. From Fig. 10, it can be seen that following mercury entrapment the width of the hysteresis loops increase in all cases. While the OC desorption isotherms for the SD feed pellets have two knees, those for the RC feed pellets only possess one. It can also be seen in Fig. 10 that the Gurvitch volumes are higher for the overcondensation data than for the conventional isotherms for all pellet types. However, the pore volume missing from the conventional adsorption isotherm is larger for the reduced pellets than for the aged pellets.

Fig. 11 shows a comparison of the conventional adsorption isotherms and overcondensation (OC) boundary desorption isotherms for empty fresh SD feed pellets and reduced SD feed pellets following mercury intrusion to 4400 psia. It can be seen that, while there are some differences in the details of the isotherms, the overall shapes of the isotherms for the fresh pellet, and reduced pellet following mercury entrapment, are similar. Both OC desorption isotherms in Fig. 11 show a more extended, initial, flat plateau at higher pressures, and sharper first desorption knee, at a relative pressure of $\sim$0.95, than observed, for the empty reduced SD pellet, and for these pellets following mercury intrusion to only 3800 psia, in Fig. 10. Both isotherms in Fig. 11 also have a second, more rounded, desorption knee at relative pressures of $\sim$0.7–0.8. Hence, while reduction has led to an increase in surface area, and thus rise in the amount adsorbed at Point B, filling the largest pores of the reduced pellet with entrapped mercury reduces the remaining void space to a structure that gives rise to a similarly-shaped isotherm to the fresh catalyst. This suggests that the reduction process largely generates new types of large macropores, as evident in the CXT data. This contrasts with the pattern of solid consolidation seen in calcination studies. Weber et al. (2022) found no changes to the connectivity of the macroporosity, while Venkatesh et al. (2023) found that the shape and spread of the pore size distribution changed little until very high pellet densities.

Table 4
Connectivity (Z) and lattice size (L) parameters from a percolation analysis of gas sorption data for (a) Aged SD pellets and (b) Aged RC pellets, both empty (Pre-Hg) and following (post) mercury intrusion to different stated pressures.

Samples	(a) Aged SD			(b) Aged RC		
	Empty pore fraction/%	Z	L	Empty pore fraction/%	Z	L
Pre-Hg	100.0	3.22	3.00	100.0	3.13	3.22
Post 2860 psia	88.1	3.05	4.62	90.4	3.01	4.52
Post 3900 psia	80.5	2.89	6.57	79.7	2.83	5.59

The conventional adsorption and overcondensation desorption isotherms for the reduced and aged catalysts were analysed using percolation theory, as described in previous work (Mousa et al., 2023). The connectivity and lattice size parameters obtained for the catalysts are shown in Tables 3 and 4. It can be seen that the connectivity declines, and the lattice size increases, with increased mercury entrapment (and thus decreasing empty pore volume). The decline in connectivity reflects the aforementioned widening of the hysteresis loops in the raw isotherm data. The rise in lattice size reflects the sharpening of the initial desorption knee with increasing mercury entrapment.

4.5. *Gas sorption pore size distributions (PSDs)*

Fig. 12(a)-(d) show the Barrett-Joyner-Halenda (BJH) (1951) pore size distributions (PSDs) of the sub-set of pores that become inaccessible from the exterior, for each stage in the series as the ultimate intrusion pressure is increased progressively in each individual porosimetry scanning curve for the reduced and aged samples. These PSD difference plots were created by subtracting PSDs from isotherms for samples collected after successive mercury scanning curves. In general, lower-pressure scanning curves fill large and medium pores, whereas higher-pressure scanning curves fill part of the remaining medium and smaller pores. As a result, access to progressively smaller pores declines as the intrusion pressure increases.

From the BJH difference PSDs in Fig. 12, the position of the peak, in the pore sizes being filled, stays the same for reduced SD and RC feed pellets, and so the critical pore size for mass transport will remain the same. However, for the aged SD and RC samples, as mercury is entrapped over pressure intervals 2860–3900 psia, the position of the peak in the pore size being filled has shifted slightly to the smaller pores, and so the critical pore size for the mass transport will change slightly.

4.6. *Rate of adsorption*

The rate of uptake of nitrogen at 77 K was measured at low pressure for empty reduced and aged pellets, and for these pellets following mercury entrapment. The mass uptake curves were fitted to the Linear Driving Force (LDF) model (Rigby, 2020) to obtain the mass transfer coefficient (MTC), denoted k. Examples of fits of such uptake data to the LDF model are shown in Appendix Fig. A2. The MTCs from the gas uptake data were corrected for adsorption using the slope of the equilibrium isotherm at the point where the mass transport experiment was conducted. Fig. 13 shows comparisons of the observed fractional decline in the mass transfer coefficient (k/k_0, where k_0 is the MTC for the empty sample) following mercury entrapment, and that expected for a random arrangement of entrapped of mercury from the Prager (1960) model, for the reduced and aged, SD and RC feed pellets. Also shown in Fig. 13, for comparison, is the experimentally observed fractional decline in the mass transfer coefficient for the fresh state of the RC and SD pellets, obtained in previous work (Mousa et al., 2023). From Fig. 13(a) it can be seen that the decline in MTC, with increasing pore volume blocked by entrapped mercury, is even more precipitous for the reduced and aged

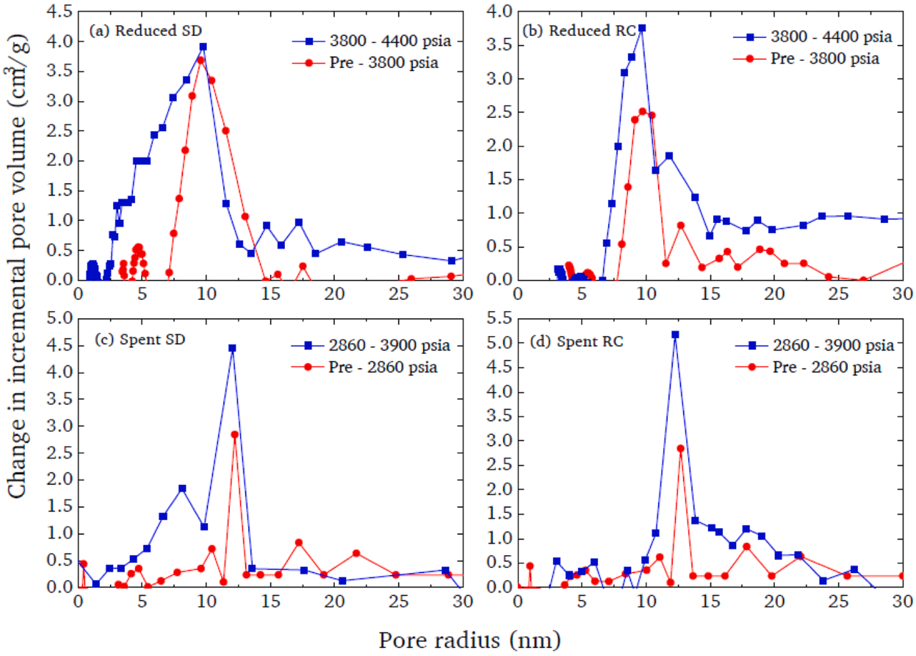

Fig. 12. BJH pore size distributions for the sub-sets of pores that become inaccessible from the exterior as the mercury intrusion pressure is increased to progressively higher ultimate pressures (as indicated in legend) for each scanning curves. (a) Reduced SD, (b) Reduced RC, (c) Aged (Spent) SD and (d) Aged RC. Pre = empty pellet.

SD pellets than for the SD fresh pellets, and much more than expected for a random arrangement of entrapped mercury. This suggests that just the relatively small volume of pores initially filled with mercury is critically important to mass transport in the network. A similar precipitous decline in MTC, with relatively small amounts of blocked pores, is also observed for the reduced RC pellets in Fig. 13(b). However, the mass transfer data for the aged RC pellets, shown in Fig. 13(b), exhibits more complex behaviour with increasing blocked pore volume. It can be seen that, after mercury entrapment blocked 9.6 % of the pore volume, the MTC for the aged RC feed pellet increased to above the initial value for the empty sample, as k/k_0 exceeds unity. Thereafter, as more pore volume is blocked, the k/k_0 value falls below that expected for a random arrangement of entrapped mercury.

5. Discussion

A comparison of both the gas sorption and mercury porosimetry pore size distributions obtained for reduced catalysts with those obtained after use in a reactor have shown that, for both RC and SD feed pellets, the modal mesopore and macropore diameters have grown following sintering of the solid. In contrast, for both the copper-silica catalysts, made by either impregnation or precipitation, studied by van den Berg et al., (2016), the macro- and meso-pore modal sizes remained more or less constant following use in the reactor, though a complete measurement of all, especially larger, macroporosity was not shown. However, nitrogen sorption accessible pore volume was lost after use in the reactor, as also seen here. Schumann et al. (2014) did not provide any detailed characterisation of the pore structure on reduction and following use.

The CXT images obtained here following mercury entrapment have shown that the reduced and aged state pellets contain macroscopic heterogeneities in the spatial distribution of porosity and pore sizes that differ substantially from those observed previously for the fresh state (Mousa et al., 2023). These new heterogeneities dominate mass transport processes in these pellets. The extent and type of changes to the macropore structure observed here, following reduction and ageing of the catalysts, contrast with those observed in some previous studies of the calcination of silica-aluminas (Tariq, Haswell et al., 2011; Tariq, Lee et al., 2011), and aluminas (Weber et al., 2022; Venkatesh et al., 2023). Sintering of the silica-aluminas led to more constrictions in the pore space, compared to the opening up of the accessibility of the void space of the methanol synthesis catalysts. For the aluminas studied by Venkatesh et al. (2023), the pore size distributions remained relatively unchanged following calcination. These differences are probably due to the additional presence of copper and zinc oxide content of the catalysts, in addition to alumina, and the more thermochemical nature of reduction and ageing, compared to just thermal calcination. However, a loss of mesoporosity (smaller pore sizes) due to matrix consolidation was seen by Weber et al. (2022) and Hondo et al. (2016), as was also seen here. Hondo et al.(2016) also found that the larger inter-granular (between feed particles) pores grew in size with increased sintering, which is more in line with what was observed in this work. Further, Hondo et al. (2016) reported that the feed particle shrinkage, giving rise to the growth in macropores, was not uniform, so the pellet microstructure evolution was heterogeneous, as was also observed in this work.

It was observed above that the MTC for methanol catalysts declined much more significantly with the loss of just ~10–15 % of pore volume for the aged and reduced SD pellets, and the reduced RC pellets, than was expected for a random arrangement of that mercury, and even that observed previously for the fresh state of these pellets (Mousa et al., 2023). This is because, as the integrated gas sorption and mercury porosimetry data has shown, the mercury entrapment occurs initially in the largest pores dominating mass transport. The CXT data for pellets following mercury entrapment have shown that many of these largest pores are the particular macroporosity induced by the reduction and sintering processes. The kinetic gas uptake experiments have thus shown that these new, induced pores provide critical transport super-highways for accessing the interior of the pellet not present, initially, in the fresh state pellets, and this new accessibility is severely impeded when these pores are blocked by mercury.

The CXT data can also explain the apparently anomalous result for mass transport following mercury entrapment for the aged RC feed pellets, where the MTC initially increased above the value for the empty pellets following some mercury entrapment. In contrast to the

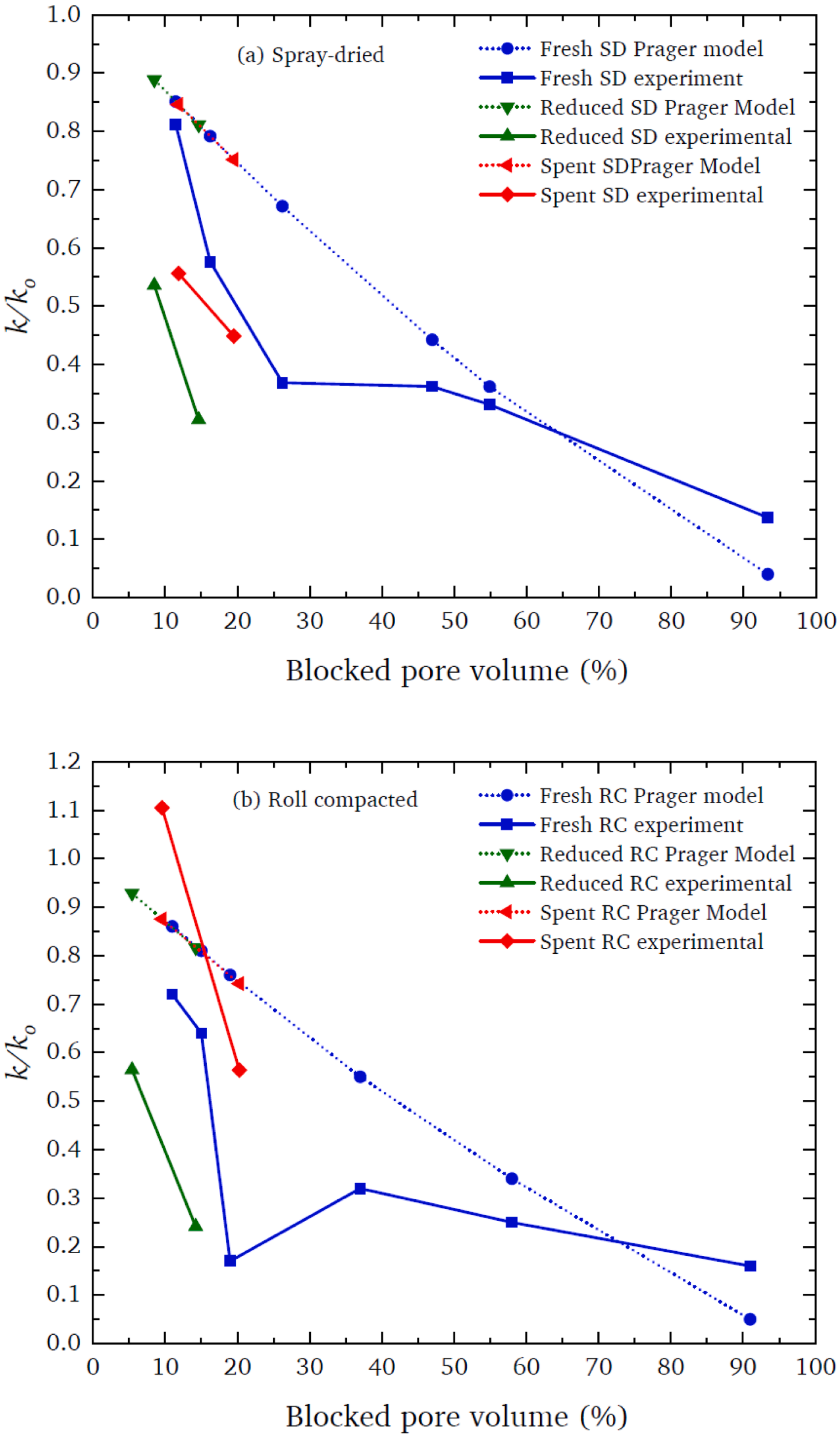

Fig. 13. Comparisons of the experimentally observed fractional decline in the mass transfer coefficient (k/k_0) following mercury entrapment, and that expected for a random arrangement of entrapped mercury from the Prager (1960) model, for (a) Fresh, Reduced and Aged (Spent) state SD feed pellets, and (b) Fresh, Reduced and Aged state RC feed pellets.

corresponding image data for other states of the pellets studied here, the CXT image for the aged RC feed sample after intrusion of mercury to 2860 psia, in Fig. 9, shows substantial amounts of mercury pervasively distributed in the core of the pellet. If this mercury cuts off access to the central core of the pellet completely then, as seen from Eq.(2), the diffusion penetration depth a would be decreased and the MTC would increase above that for the completely empty sample, as observed.

As mentioned above, a simple percolation model was able to predict

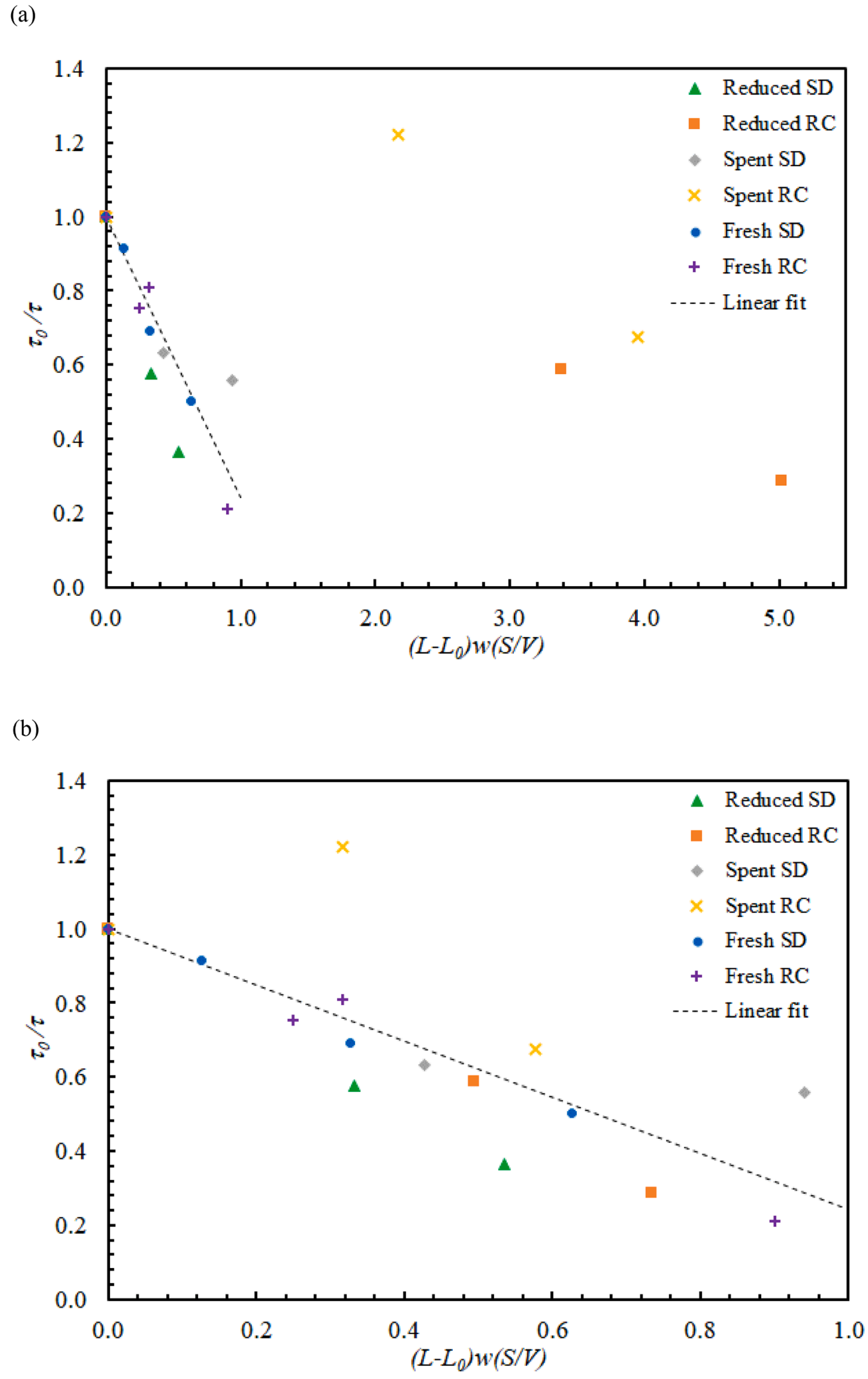

Fig. 14. Fits of the experimental gas sorption data against the percolation theory lattice model described by Eq. (4) for a characteristic particle size w of (a) 1300 µm for all RC pellets, and (b) 190 µm for the aged (spent) and reduced RC feed pellets. The particle size w was kept fixed at 200 µm for all the SD feed pellet data. The dashed line is a fit of the data to Eq. (4) with gradient (±1 std. err. (SE)) = -0.76 ± 0.12, intercept (±1SE) = 1.00 ± 0.05, and adjusted r^2 = 0.7.

the relative change in tortuosity, τ, as more of the void space was blocked by entrapped mercury in fresh state pellets, such that (Mousa et al., 2023):

$$\frac{\tau_0}{\tau} = 1 - \gamma(L - L_0)w\frac{S}{V}, \tag{4}$$

where the subscript 0 indicates the variable value for the empty pellet, L is the apparent lattice size (from percolation analysis of the gas sorption data), w is the characteristic pellet feed particle size, S/V is the surface area-to-volume ratio of the pellet, and γ is a geometric factor (typically close to unity) quantifying the difference in shape for constituent feed particles and pellet. The new data obtained for the aged and reduced pellets has been plotted in the form of Eq. (4) in Fig. 14(a), assuming that the critical pore size for the pore diffusivity did not change following entrapment, and the feed particle size w was the same for all the RC and SD feed pellets as for the corresponding fresh state pellets of 1300 and

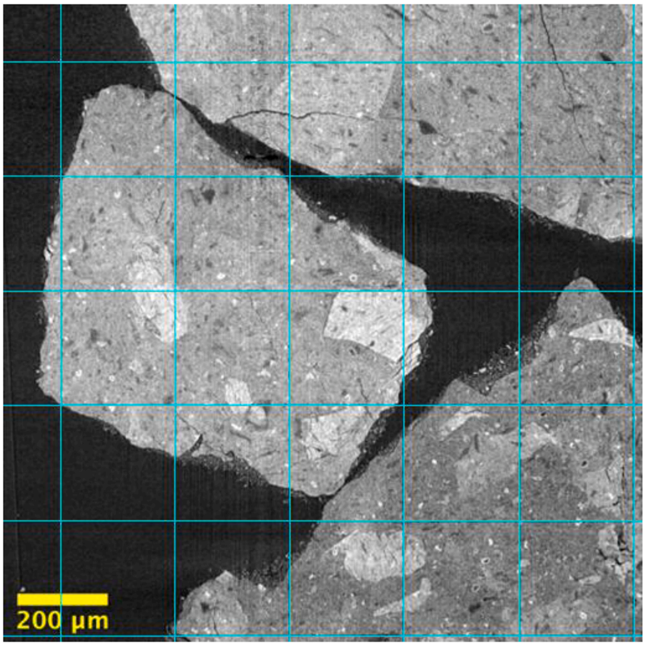

Fig. 15. A high resolution, 2D cross-sectional CXT image of a typical roll-compacted feed particle before compaction. The image has been overlain with a square grid of spacing of 250 μm.

200 μm, respectively. From Fig. 14(a), it can be seen that, while the new data for the reduced and aged SD feed pellets fits a similar linear trend, as expected from Eq. (4), as do both types of fresh state pellet seen previously (Mousa et al., 2023), in contrast, the corresponding data for the reduced and aged RC feed pellets are shifted to larger values of the abscissa variable. However, as seen in Fig. 14(b), if the value of *w* for the reduced and aged RC feed pellets is modified downwards to 190 μm, then these data now lie better along the same trend as all the other data for the other types of pellet. The fit of all of the pellet data to Eq.(4) is statistically-significant ($F = 42.9, p = 4 \times 10^{-6}$), but there is more scatter about the straight-line trend for the reduced and aged catalyst data, than for the fresh state data, but this may be because of slight changes in the critical pore size with mercury entrapment mentioned above. The outlier data-point for the aged RC pellet, at τ_0/τ of 1.22, can be made to fit the linear trend better if it is assumed that the diffusion penetration depth *a* is reduced to ~ 85 % of the original.

A comparison of the CXT data for the original RC feed particles and aged RC feed pellets following mercury entrapment reveals the structural changes, occurring during reduction and over time on-stream in the reactor, that are responsible for the change in effective *w*-value. Fig. 15 shows a high resolution, 2D cross-sectional CXT image of a typical roll-compacted feed particle before compaction. The image has been overlain with a square grid of side-length 250 μm. It can be seen that the RC feed particles are themselves composite structures, composed of irregular fragments of variable density (as shown by the differences in image voxel intensity, and, thence, X-ray absorbance), of characteristic sizes similar to the grid side-length. Image analysis was conducted on images like Fig. 15, and an average particle size for the constituent regions of the RC feed was found to be close to ~238 μm.

Fig. 16 shows a CXT 2D cross-sectional image through an aged pellet, tabletted with roll compacted feed, containing entrapped mercury following intrusion up to 2860 psia. The image has been overlaid with gridlines with separations the same as the original RC feed size of 1300 μm, and also with gridline separation of 250 μm, similar to the measured constituent fragment sizes for the RC feed particles found above. The brightest intensity (white) image voxels are those regions containing entrapped mercury. The separations of the bright white intensity regions and lines in Fig. 16 tend to be smaller than the gridline spacing of 1300 μm in Fig. 16(a). However, in Fig. 16(b), it can be seen that, in many places in the image, the bright white voxels form fuzzy lines that enclose regions of the image of overall size similar to the 250 μm grid-spacing, or thereabouts. This suggests that the solid shrinkage following the reduction and sintering processes has led to the emergence of the constituent fragments within the RC feed particles as the characteristic length-scale, determining mass transport, for the overall pellet structure, rather than that of the larger composite feed particle, as for the fresh state. This is consistent with the results in Fig. 14(b) that suggest that it is the constituent fragments of the RC feed that, after reduction, form the fundamental underlying unit of the percolation lattice, as the value of *w* is consistent with the sizes of the constituent fragments seen in Fig. 15. In comparison, the typical spacing of the induced macropores for the SD feed pellets, as seen in Figs. 1, 2 and 7, is much larger than the original SD feed particle spheres, and, thus, does not affect *w*.

The CXT images of the reduced and aged catalyst pellets following mercury porosimetry show why the simple bond percolation lattice model works for predicting the change in tortuosity with mercury entrapment. As was seen for the fresh state pellets, mercury becomes entrapped in clusters of large pores that reach the surface of the pellet. This is particularly apparent from the entrapped mercury clearly evident at the sides of the pellets in Figs. 7, 8 and 9. The importance of the surface clusters of larger pores is especially evident for the aged RC feed pellets. While the CXT image of the centre of the pellet in Fig. 9 suggests

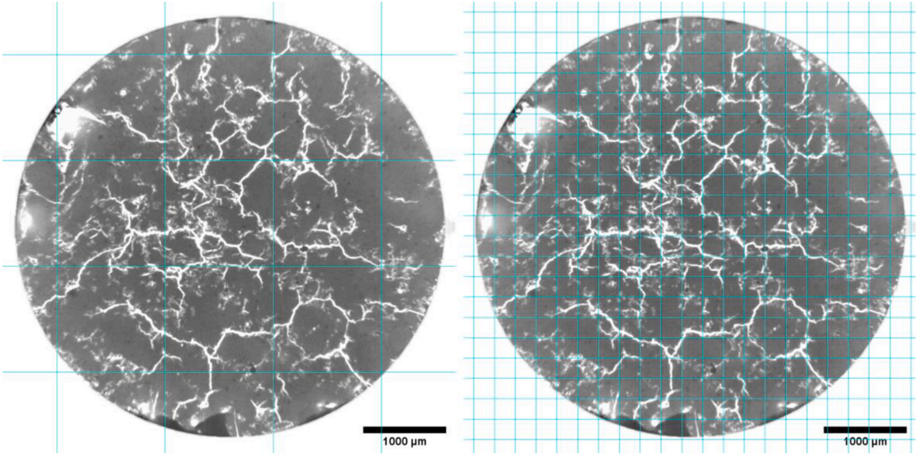

Fig. 16. CXT 2D cross-sectional image of the periphery of an aged roll compacted feed pellet sample with mercury entrapment following intrusion up to 2860 psia, together with a grid of lines overlaid on the images. The grid spacing per square on each image is (a) 1300 μm, and (b) 250 μm. The scale bar corresponds to 1 mm.

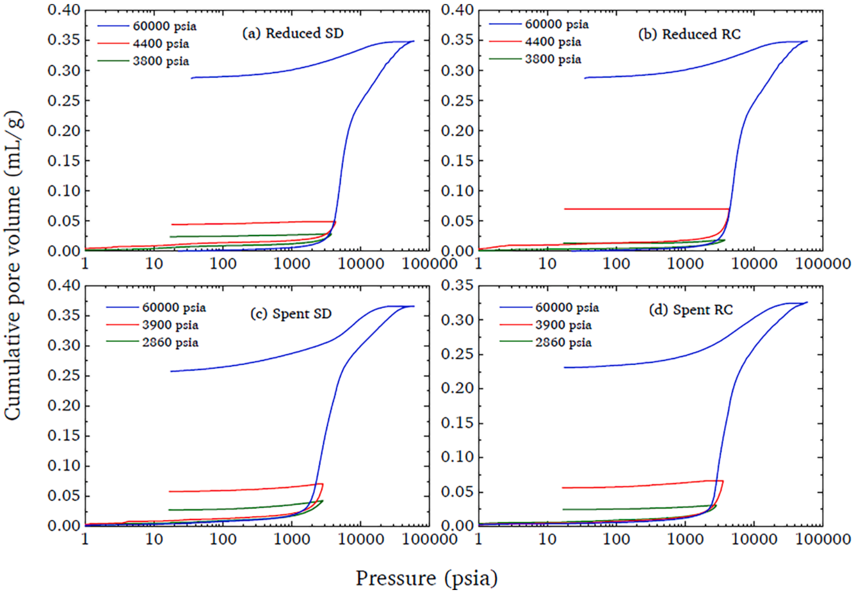

Fig. A1. Raw mercury porosimetry scanning curve data for (a) Reduced SD, (b) Reduced RC, (c) Aged (Spent) SD and (d) Aged RC. The mercury scanning curve pressures are indicated on the graph legends.

that mercury can pervasively permeate the whole of the core region once there, the edges of this same image, and also that of the pellet periphery in Fig. 16, show that overall accessibility of the pellet interior is controlled by the surface clusters of induced macropores. Once these regions at the sides of the pellets become blocked with entrapped mercury, this means that the apparent ratio of the external surface area-to-pellet volume declines, as would also occur if the original pore network had been made larger overall. Hence, the apparent lattice size of the percolation model (in Tables 3 and 4) increases. The fundamental, dimensionless length-scale in the pellet *w(S/V)* determines the 'conversion factor' between the model lattice unit and the real pellet. It has, thus, been suggested, by the findings here, that this critical length-scale, for the structural element governing mass transport, is changed by the later processing stages of the catalyst, and this element has been identified using the 'sifting' strategy.

6. Conclusions

The 'pore-sifting' technique has shown that the particular, new macroporosity induced in the catalyst pellets by reduction and sintering substantially dominates mass transport thereafter, since its loss leads to a much more precipitous decline in mass transfer rates compared to a similar fractional loss of pore volume in the fresh state. The combination of gas overcondensation data and CXT images has been found to contain sufficient pore structural information to predict consequent changes to mass transfer rates following controlled changes to the pore structure. The macropores induced by reduction and sintering form surface clusters such that the simple bond percolation lattice model can successfully

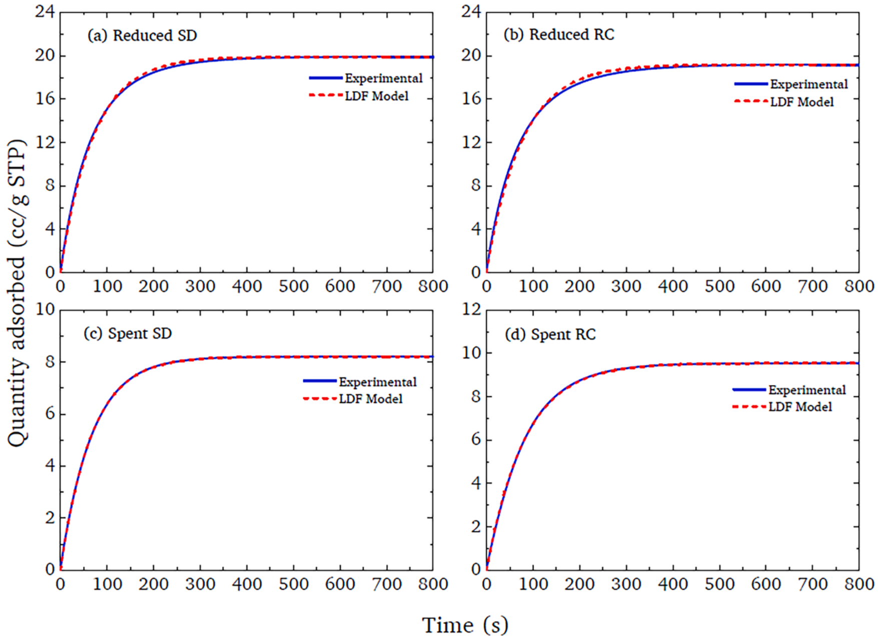

Fig. A2. A comparison of the experimental raw nitrogen gas uptake data and the fits to the linear driving force (LDF) model for the empty reduced SD, reduced RC, Aged (Spent) SD, and Aged RC pellets.

predict the impact of their knock-out from the network, with entrapped mercury, as it could for fresh state pellets.

The novel prediction, of the change in the key structural element for aged RC pellets, by the percolation model shows that the sifting strategy duly selects the critical aspect(s) of the pellet to incorporate into a structural representation. This confirms the theory behind the sifting strategy that underlying the full structural complexity of the pellet is a simpler, key network of critical elements that control mass transport that can be revealed by the pore-sifting procedure. The CXT images and percolation model have, together, suggested that reduction and sintering leads to a change, compared to fresh pellets, in the fundamental fabrication process parameter, critical for determining mass transport in pellets formed with roll-compacted feed, from composite feed particle size to constituent fragment size.

Declaration of Competing Interest

The authors declare that they have no known competing financial interests or personal relationships that could have appeared to influence the work reported in this paper.

Data availability

The data that has been used is confidential.

Acknowledgements

This work was supported by the Engineering and Physical Sciences Research Council [grant numbers EP/R512059/1 and EP/S021434/1]. VN acknowledges funding from the European Union’s Horizon 2020 research and innovation programme under the Marie Skłodowska-Curie Grant Agreement No 701647. We acknowledge the Paul Scherrer Institut, Villigen, Switzerland, for providing synchrotron radiation beamtime at the TOMCAT beamline X02DA of the SLS. We thank Martin Corfield for help with producing the lower resolution CXT images.

Appendix

References

Arif, M., Mahmoud, Y., Zhang, S., Iglauer, S., 2020. X-ray tomography imaging of shale microstructures: a review in the context of multiscale correlative imaging. Int. J. Coal Geol. 233, 103641.

Bare, S.R., Charochak, M.E., Kelly, S.D., Lai, B., Wang, J., Chen-Wiegart, Y.K., 2014. Characterization of a fluidized catalytic cracking catalyst on ensemble and individual particle level by X-ray micro- and nanotomography, micro-X-ray fluorescence and micro X-ray diffraction. ChemCatChem 6, 1427–1437.

Barrett, E.P., Joyner, L.G., Halenda, P.P., 1951. The determination of pore volume and area distributions in porous substances. I. Computations from nitrogen isotherms. J. Am. Chem. Soc. 73 (1), 373–380. https://doi.org/10.1021/ja01145a126.

Carniglia, S., 1986. Construction of the tortuosity factor from porosimetry. J. Catal. 102 (2), 401–418.

Epstein, N., 1989. On tortuosity and the tortuosity factor in flow and diffusion through porous media. Chem. Eng. Sci. 44 (3), 777–779.

Fu, J., Thomas, H.R., Li, C., 2021. Tortuosity of porous media: Image analysis and physical simulation. Earth Sci. Rev. 212, 103439.

Fusi, N., Martinez-Martinez, J., 2013. Mercury porosimetry as a tool for improving quality of micro-CT images in low porosity carbonate rocks. Eng. Geol. 166, 272–282.

Ghanbarian, B., Hunt, A.G., Ewing, R.P., Sahimi, M., 2013. Tortuosity in porous media: a critical review. Soil Sci. Soc. Am. J. 77 (5), 1461–1477.

Hill-Casey, F., Hotchkiss, T., Hardstone, K.A., Hitchcock, I., Novak, V., Schlepütz, C.M., Meersmann, T., Pavlovskaya, G.E., Rigby, S.P., 2021. Hyperpolarised xenon MRI and time-resolved X-ray computed tomography studies of structure-transport relationships in hierarchical porous media. Chem. Eng. J. 405, 126750.

Hondo, T., Kato, Z., Yasuda, K., Wakai, F., Tanaka, S., 2016. Coarse pore evolution in dry-pressed alumina ceramics during sintering. Adv. Powder Technol. 27 (3), 1006–1012.

Kloubek, J., 1981. Hysteresis in porosimetry. Powder Technol. 29, 63–73.

Makovetsky, R., Piche, N., Marsh, M., 2018. Dragonfly as a platform for easy image based Deep Learning applications. Microsc. Microanal. 24 (S1), 532–533.

Marone, F., Stampanoni, M., 2012. Regridding reconstruction algorithm for real time tomographic imaging. J. Synchrotron Radiat. 19, 1029–1037.

Mousa, S., Novak, V., Fletcher, R.S., Garcia, M., Macleod, N., Corfield, M., Rigby, S.P., 2023. Integration of multi-scale porosimetry and multi-modal imaging in the study of structure-transport relationships in porous catalyst pellets. Chem. Eng. J. 452, 139122.

Murray, K.L., Seaton, N.A., Day, M.A., 1999. An adsorption-based method for the characterization of pore networks containing both mesopores and macropores. Langmuir 15 (20), 6728–6737.

Nepryahin, A., Fletcher, R.S., Holt, E.M., Rigby, S.P., 2016. Structure-transport relationships in disordered solids using integrated rate of gas sorption and mercury porosimetry. Chem. Eng. Sci. 152, 663–673.

Paganin, D., Mayo, S.C., Gureyev, T.E., Miller, P.R., Wilkins, S.W., 2002. Simultaneous phase and amplitude extraction from a single defocused image of a homogeneous object. J. Microsc. 206, 33–40.

Prager, S., 1960. Diffusion in inhomogeneous media. J. Chem. Phys. 33 (1), 122–127.

Qi, Y., Liu, K., Peng, Y.u., Wang, J., Zhou, C., Yan, D., Zeng, Q., 2021. Visualization of mercury percolation in porous hardened cement paste by means of X-ray computed tomography. Cem. Concr. Compos. 122, 104111.

Qian, R., Zhang, Y., Liu, C., Yang, L., Liu, G., She, W., 2018. Quantitative characterization of three-dimensional pore structure in hardened cement paste using X-ray microtomography combined with centrifuge driven metal alloy intrusion. Mater Charact 145, 277–283.

Rigby, S.P. (Ed.), 2020. Structural Characterisation of Natural and Industrial Porous Materials: A Manual. Springer International Publishing, Cham.

Rigby, S.P., Fletcher, R.S., Riley, S.N., 2004. Characterisation of porous solids using integrated nitrogen sorption and mercury porosimetry. Chem. Eng. Sci. 59 (1), 41–51.

Rigby, S.P., Watt-Smith, M., Fletcher, R., 2004. Simultaneous determination of the pore-length distribution and pore connectivity for porous catalyst supports using integrated nitrogen sorption and mercury porosimetry. J. Catal. 227 (1), 68–76.

Rigby, S.P., 2023. The Anatomy of Amorphous, Heterogeneous Catalyst Pellets. Materials 16, 3205.

Ronneberger, O., Fischer, P., Brox, T., 2015. U-Net: Convolutional Networks for Biomedical Image Segmentation. International Conference on Medical image, 9351, 234–241.

Ruffino, L., Mann, R., Oldman, R., Stitt, E.H., Boller, E., Cloetens, P., DiMichiel, M., Merino, J., 2005. Using x-ray microtomography for characterisation of catalyst particle pore structure. Can. J. Chem. Eng. 83 (1), 132–139.

Schumann, J., Lunkenbein, T., Tarasov, A., Thomas, N., Schlögl, R., Behrens, M., 2014. Synthesis and characterisation of a highly active Cu/ZnO: Al catalyst. ChemCatChem 6 (10), 2889–2897.

Seaton, N.A., 1991. Determination of the connectivity of porous solids from nitrogen sorption measurements. Chem. Eng. Sci. 46 (8), 1895–1909.

Seely, R., Liddy, T.J., Rochelle, C.A., Fletcher, R.S., Rigby, S.P., 2022. Evolution of the mineralogy, pore structure and transport properties of Nordland Shale following exposure to supercritical carbon dioxide. J. Pet. Sci. Eng. 213, 110466.

Tariq, F., Haswell, R., Lee, P.D., McComb, D.W., 2011a. Characterization of hierarchical pore structures in ceramics using multiscale tomography. Acta Mater. 59 (5), 2109–2120.

Tariq, F., Lee, P.D., Haswell, R., McComb, D.W., 2011b. The influence of nanoscale microstructural variations on the pellet scale flow properties of hierarchical porous catalytic structures using multiscale 3D imaging. Chem. Eng. Sci. 66 (23), 5804–5812.

Twigg, M.V., 2014. The Catalyst Handbook, second ed. CRC Press, Taylor & Francis Group, Boca Raton, FL.

van den Berg, R., Zecevic, J., Sehested, J., de Helveg, S., Jongh, P., de Jong, K.P., 2016. Impact of the synthesis route of supported copper catalysts on the performance in the methanol synthesis reaction. Catal. Today 272, 87–93.

Venkatesh, A.M., Bouvard, D., Lhuissier, P., Villanova, J., 2023. 3D analysis of ceramic powder sintering by synchrotron X-ray nano-tomography. J. Eur. Ceram. Soc. 43 (6), 2553–2563.

Weber, S., Diaz, A., Holler, M., Schropp, A., Lyubomirskiy, M., Abel, K.L., Kahnt, M., Jeromin, A., Kulkarni, S., Keller, T.F., Gläser, R., Sheppard, T.L., 2022. Evolution of hierarchically porous nickel alumina catalysts studied by X-ray ptychography. Adv. Sci. 9 (8), 2105432.

Weisberg, M., 2013. Simulation and Similarity: Using Models to Understand the World. Oxford University Press, Oxford, UK.

Zeiler, M.D., 2012. Adadelta: an adaptive learning rate method. Computing Research Repository, 121, arXiv: 1212.5701.

Zeng, Q., Chen, S., Yang, P., Peng, Y.u., Wang, J., Zhou, C., Wang, Z., Yan, D., 2020. Reassessment of mercury intrusion porosimetry for characterizing the pore structure of cement-based porous materials by monitoring the mercury entrapments with X-ray computed tomography. Cem. Concr. Compos. 113, 103726.